Assessment of Turbulent Shock-Boundary Layer Interaction Computations Using the OVERFLOW Code

A. B. Oliver*, R. P. Lillard†, A. M. Schwing‡, G. A. Blaisdell§, and A. S. Lyrintzis¶
School of Aeronautics and Astronautics
Purdue University
West Lafayette, IN 47907

The performance of two popular turbulence models, the Spalart-Allmaras model and Menter's SST model, and one relatively new model, Olsen & Coakley's Lag model, are evaluated using the OVERFLOW code. Turbulent shock-boundary layer interaction predictions are evaluated with three different experimental datasets: a series of 2D compression ramps at Mach 2.87, a series of 2D compression ramps at Mach 2.94, and an axisymmetric cone-flare at Mach 11. The experimental datasets include flows with no separation, moderate separation, and significant separation, and use several different experimental measurement techniques (including laser doppler velocimetry (LDV), pitot-probe measurement, inclined hot-wire probe measurement, preston tube skin friction measurement, and surface pressure measurement). Additionally, the OVERFLOW solutions are compared to the solutions of a second CFD code, DPLR. The predictions for weak shock-boundary layer interactions are in reasonable agreement with the experimental data. For strong shock-boundary layer interactions, all of the turbulence models overpredict the separation size and fail to predict the correct skin friction recovery distribution. In most cases, surface pressure predictions show too much upstream influence, however including the tunnel side-wall boundary layers in the computation improves the separation predictions.

I. Introduction

A useful computational fluid dynamics (CFD) tool for the Space Shuttle and future space vehicles needs to accurately predict the surface heat transfer over the entire vehicle, including any localized effects due to protuberances or shock wave-boundary layer interactions (SWBLIs). The acreage flow (where the variations in geometry are relatively gradual) is generally attached, so for these regions, the CFD code will be required to accurately model turbulent boundary layers. Perhaps more importantly, however, the flow around protuberances generates shock-boundary layer interactions that can produce localized peaks in the heating rates that may be several times larger than the acreage heating levels.

Advances in computer speeds have given rise to advances in high accuracy methods of simulating and modeling turbulent flows. However, grid requirements typically restrict direct numerical simulations (DNS) and even large eddy simulations (LES) to low Reynolds numbers. For complex configurations such as the Space Shuttle, grid requirements and the need for time accurate solutions make DNS and LES impractical. Although DNS and LES employ a more physics based representation of the fluid dynamics, the RANS equations, along with a turbulence model, are still a valuable tool for aerodynamic analysis.

The present work continues the development of modeling high-speed compressible flows over complex vehicles. The goal of the current project is to evaluate the performance of a set of baseline turbulence

*Graduate Research Assistant, Student Member AIAA
†PhD Candidate, Student Member AIAA; Aerospace Engineer, NASA/JSC, Aerosciences and CFD Branch
‡Undergraduate Research Assistant, Student Member AIAA
§Associate Professor, Senior Member AIAA
¶Professor, Associate Fellow AIAA.

models using the OVERFLOW code[1,2] for high-speed, non-reacting flow. The idea of using OVERFLOW as an aerothermal analysis tool has received some criticism based on the fact that it was designed to compute aerodynamic forces in transonic and low supersonic flows. Previous work[3,4] has indicated that the code is indeed capable of accurately modeling laminar hypersonic flows and does an adequate job of capturing heat transfer at those speeds in some simple cases. The present study is now directing attention at validating the use of OVERFLOW for high-speed turbulent flows by benchmarking OVERFLOW predictions against experimental data and a similar CFD code, DPLR.

Three turbulence models in OVERFLOW will be considered in this paper: the Spalart-Allmaras model,[5] the SST model,[6] and the lag model.[7] Results from each model will be compared to several different experiments and DNS computations in order to benchmark their behavior with canonical flows. Surface properties, such as surface pressure, skin friction, and heat transfer, are the primary variables of interest; however, to aid in the development and implementation of improved models and model corrections, profiles of flow variables and turbulent quantities will also be generated. Based on the results of this work, future studies will consider modifications to these turbulence models in order to improve their accuracy.

II. Test Cases

In order to assess the code's ability to capture a high-speed zero pressure gradient boundary layer, several flat plate cases have been run. Also, two-dimensional compression ramp experiments and axisymmetric cone-flare experiments were selected to analyze the shock/boundary layer interaction behavior, namely the size of the separated region, the profiles of mean velocity and turbulence quantities downstream of the shock, and the quality of the prediction of surface pressure, skin friction and heat transfer in the recovering boundary layer. Since experiments often have to make some compromises in terms of what measurements can be made, multiple experiments have been chosen for these geometries to capture specific features of the turbulent boundary layers. The experiments have been chosen based on available experimental data, perceived quality of the data, and Mach number of interest.

A. Flat Plates

In order to address several relevant features of a high-speed zero pressure gradient boundary layers, three datasets have been selected for comparison. Experimental studies by Cary[10] at Mach 6.0 and Mach 4.9 have been chosen for surface heating data. A DNS simulation by Gatski[11,12] provides detailed profiles of mean and turbulent properties. Finally, experiments conducted at the Princeton Gas Dynamics Lab[13,14] at Mach 2.87 have profiles at multiple locations upstream of 8° and 16° compression corners, and will be used for comparison of high Reynolds number experimental velocity profiles and boundary layer growth measurements. This paper will present the results for the shock/boundary layer interaction datasets. The zero pressure gradient results have been published previously.[8,9]

B. Compression Ramps

Two supersonic compression ramp datasets with freestream Mach numbers near 2.9 have been chosen for comparison. The experiments of Kuntz[15–17] provide two component laser doppler velocimetry (LDV) measurements of turbulent boundary layers on ramps of 8°, 12°, 16°, 20°, and 24°, and the series of experiments[13,14] conducted at the Princeton Gas Dynamics Laboratory will be used to compare turbulence quantities downstream of the shock and for skin friction and surface pressure distributions on ramps of 8°, 16°, 20°, and 24°.

There are a few common problems with these datasets that should be explicitly noted. First of all, it should be noted that the two-dimensionality assumption is a rather large assumption, and it does not necessarily hold for the the larger ramp angles. Additionally, both of the datasets use ramp models attached to the floor of the wind tunnel, so the turbulent boundary layers had previously experienced a strong distortion through the nozzle. The effect this had on the turbulence is unknown. Finally, Settles and Dodson report in their 1994 shock-boundary layer interaction database[18] that these two datasets disagree on the magnitude of the Reynolds stresses by as much as a factor of 4. To date, the authors are not aware of an explanation for this discrepancy, so following the suggestion of Settles and Dodson, these values are taken to be reasonable bounds of the actual Reynolds stresses.

Despite these problems (and a few ones particular to each dataset described below), these two datasets appear to be the most rigorous experiments to cover a large range of interaction strengths in the same experiment. To help alleviate some uncertainty, work is presently underway to study the sensitivity of the solutions to the 3D end effects. Preliminary results from this end-effects study will be shown.

1. Princeton

Several researchers conducted a series of compression corner experiments in the Princeton 20 cm × 20 cm high Reynolds number supersonic wind tunnel. A significant number of parameters were studied in this series of experiments; however, only a subset of this data will be considered here. A description of these selected experiments follows.

The ramp angles considered (8°, 16°, 20°, and 24°) provide flows that range from unseparated to significantly separated. The 6 inch wide compression ramp models were mounted on the wind tunnel floor with one inch of clearance on either side to permit the passage of the sidewall boundary layers. The ramp model station was located far enough downstream of the nozzle that the turbulence in the boundary layer appeared to have fully recovered from distortion in the nozzle. The boundary layer was nominally 26 mm thick ($\theta = 1.3$ mm) upstream of the ramp corner location, although the specific values varied for each case. The freestream Reynolds number was approximately $6.3 \times 10^7\ m^{-1}$, which gives $Re_\theta = 7.8 \times 10^4$, two inches upstream of the ramp corner. The temperature of the tunnel walls and ramp models was not controlled; however, the temperature was observed to be approximately 1.05 times the stagnation temperature (hot-wall conditions). A summary of the case specific conditions is given in Table 1.

Settles et al.[13] analyzed the mean flowfields using several methods. Pitot and static pressure probes were used to make measurements of mean velocity in the boundary layers upstream, inside, and downstream of the interaction. Static pressure measurements were made on the surfaces of all models, and Preston tubes were used to measure skin friction. Surface streak and schlieren photography were used to observe separation behavior. Two dimensionality of the flow was verified with surface streak measurements (aerodynamic fences were necessary for the higher ramp angles to achieve two dimensionality). Interference effects due to the various probes were assessed with schlieren photos, surface pressure measurements, and surface streak observations.

Smits et al.[14] revisited the Settles et al.[13] dataset and added to it by using hot-wires to measure fluctuating quantities. It does not appear that Smits et al. repeated any new mean flow measurements (likely because the flow conditions were not significantly different from those used by Settles et al.) and used the Settles et al. measurements in their data reduction process (see note on page 64 of reference[19]). Single normal hot-wires were used to measure the normal Reynolds stresses and longitudinal mass flux fluctuations; inclined wires were used to measure Reynolds shear stresses. Evans et al.[20] instrumented the 16° ramp with thin-film gages and measured heat transfer from the surface of the ramp in the recovering boundary layer. These runs deviate from the Settles et al. flow conditions more than the Smits et al. runs, as the wall temperature increased by 13 K (5%). The Settles et al.[13] dataset and the Smits et al.[14] datasets are both listed as acceptable experiments in the Settles and Dodson database,[18,19] and the Settles et al.[13] dataset is included in the 1980-81 AFOSR-HTTM-Stanford Conference on Complex Turbulent Flows.[21]

2. Kuntz

Kuntz et al.[15–17] conducted a series of compression corner SWBLI experiments using a non-intrusive two-component LDV system to measure flow velocity and turbulence properties. The range of ramp angles were chosen to span the full range of possibilities: flows with no separation, incipient separation, and significant separation. The ramp models were located on the floor of a 10.2 cm × 10.2 cm blow-down wind tunnel, and spanned the entire width of the tunnel test section. The Mach number in the test section was determined to be 2.94 based on surface static pressure measurements, and two-dimensionality was determined via observation of surface-streak patterns. Three-dimensionality was observed in the 16°, 20°, and 24° cases, but the reattachment line was reportedly straight for the inner 7 cm of the 10.2 cm test section width. The stagnation pressure was approximately 483 kPa (70 psia), and the total temperature varied from 21°C to 29°C (the room temperature of the facilities). Given the short run times (90 seconds max) and the thick aluminum construction, the walls likely approximated isothermal walls near the stagnation temperature.[22]

Incoming boundary layer properties were measured using the LDV system in the tunnel without a ramp model in place. The no-ramp setup was also used to determine the freestream conditions. These runs

determined that the boundary layer at the corner location was 8.27 mm thick (based on 99% of freestream velocity), and numerical integration of the compressible profiles (assuming adiabatic behavior of the boundary layer to determine density) yielded displacement and momentum thicknesses of 3.11 mm and 0.57 mm, respectively. The Reynolds number based on boundary layer thickness was $Re_{\delta_0} = 3.1 \cdot 10^5$ ($Re_\theta = 2.2 \cdot 10^4$). The profiles were least-squares fit to find the wake strength parameter, Π, and the skin friction, C_f, using the transformed wall-wake law presented by Maise and McDonald.[23] This fit found $\Pi = 0.98$ and $C_f = 0.00114$ for the undisturbed boundary layer. Kuntz[17] says that the value of the wake strength parameter is rather large, but agrees with several other experiments. Table 1 provides the detailed flow conditions reported for this series of experiments.

Schlieren photography was used to ensure the entire flow was supersonic for each model, and some unsteadiness in the shock was observed. Separation was observed in the 16°, 20°, & 24° corners with both Schlieren photography and surface streak measurements. It was observed that lengths of all but the 24° ramp were long enough to permit full pressure recovery. However, the ramp lengths were not long enough to permit the turbulence to return to an equilibrium state after passing through the shock.

Settles and Dodson reported in[19] that the boundary conditions were not clear and that the LDV data may be inconsistent. This paper only references the AIAA journal article.[15] The experiment was tagged unacceptable. However, in Reference,[18] they change their minds about this dataset and label it as acceptable. They note, however, that the magnitudes of the Reynolds stresses measured with the LDV system are 2 to 4 times larger than the values reported by Smits et al.[14] using hot-wires. Kuntz et al.[17] speculate that difficulties calibrating inclined hot-wires are responsible for the discrepancy. However, the actual source of the discrepancy is not known. Settles and Dodson[18] decided to include both datasets to provide an idea of the reasonable limits of Reynolds shear stress in this class of flow.

C. Cone-Flare

One major drawback to the two-dimensional plane compression ramp is that the flow is not exactly two dimensional; end effects are always present and their influence on the interaction is likely very complicated. An axisymmetric cone-flare model at zero angle of attack alleviates this problem.

The dataset obtained by Holden et al.[24] reports heat transfer and surface pressure measurements on two cone-flare models in Mach 11 flow in the Calspan 96-inch shock tunnel. These models used a 9 foot (4.12 m) long 6° cone to generate a turbulent boundary layer with natural transition. Flares with angles of 36° and 42° (measured from the axis of symmetry) attached to the end of the cone result in compression-corner SWBLIs that are unseparated and separated, respectively. The freestream Reynolds number outside the conical shock wave is $Re_\infty = 3.30 \cdot 10^5$ in^{-1}.

There is a fair amount of uncertainty surrounding this dataset at the time of this writing. Only one paper has been found that describes this dataset, although the data also appears in electronic format in the Settles and Dodson database (the database description outlines the cone-flare experiments; however, the references it cites describe three-dimensional swept shock boundary layer interaction experiments). The experimental boundary layer thickness is not explicitly stated in the paper (although it appears as a note in one of the plots). The wall temperature is not stated, so room temperature was assumed. Likewise, the exact model geometry is not provided; however, the geometry is given in the Settles and Dodson description of the experiment. Finally, the freestream stagnation conditions are not explicitly stated and had to be backed out from the stagnation values prior to the shock heating (the paper describes how to do this).

Despite these issues, this test case is still briefly considered in this study. The heat transfer data shows significant heating at the reattachment point, a common and important feature of SWBLI's that is not addressed by the Mach 3 compression corner experiments.

III. Numerical Methods

A. Code Description

The OVERFLOW code is an overset grid (chimera) Navier-Stokes solver, which makes it ideal for computing the flow fields over complex geometries.[25] It uses a finite-difference formulation with flow quantities stored at the grid nodes. OVERFLOW has central- and Roe upwind-difference options, and uses a diagonalized, implicit approximate factorization scheme for time advancement. Local timestepping, multigrid techniques and grid sequencing are all used to accelerate convergence to a steady state solution. In the present study, the

Swanson/Turkel matrix dissipation model[26] was utilized. With the appropriate parameters,[3] this allows the central-differenced scheme to mimic a Total Variation Diminishing (TVD) upwind biased scheme in regions of flow discontinuities. This method takes advantage of the speed of central differencing while maintaining the robustness of the upwind TVD scheme. For a complete discussion of the scheme, see Olsen et al.[3]

B. Turbulence Models

OVERFLOW has numerous turbulence models coded in, but this study focuses on the two most popular turbulence models in the OVERFLOW code: the Spalart-Allmaras (SA) model and the SST model, and also on a promising new model: the lag model. All three of these turbulence models make use of the Boussinesq approximation, meaning that the effects of the Reynolds stress terms are included in the Navier-Stokes equations through an eddy viscosity. Each of the test cases is computed with all three turbulence models to allow comparisons of the models.

1. Spalart-Allmaras (SA) Model

The SA model[5] is a one-equation turbulence model developed specifically for aerodynamic applications. Being a one-equation turbulence model, it only needs to solve one partial differential equation to find the eddy viscosity. It is popular for design use because of its simplicity, low cost (low grid resolution requirements near wall), and robustness for aerodynamic flows. It has been shown[27] to be capable of providing accurate results in the hypersonic regime and is one of the most commonly used turbulence models in OVERFLOW. The specific implementation of the SA model in the OVERFLOW code makes use of loose coupling and first order accurate spatial derivatives.

2. Menter's SST Model

The SST model[6] is a two-equation model which is a hybrid of the k-ϵ and k-ω turbulence models and solves partial differential equations for the turbulent kinetic energy and the specific dissipation rate. The eddy viscosity is then derived from an algebraic relation that chooses the minimum value between the standard formulation (based on the turbulence kinetic energy and the specific dissipation rate) and a formulation based on an assumed value of the normalized Reynolds shear stress. This hybrid formulation is popular for aerodynamic design and analysis because it retains the accuracy of the k-ω near-wall behavior and the k-ϵ wake region behavior.

3. Olsen & Coakley's Lag Model

The Lag model[7,28] is a recent extension of the k-ω model[29] that accounts for non-equilibrium effects by carrying an additional differential equation that relaxes the eddy viscosity to the equilibrium value. This third equation accounts for the time required for the turbulence to respond to changes in the mean flowfield. This model is based on the 1998 $k-\omega$ model, except that the eddy viscosity, ν_t, is given by a field PDE, instead of k/ω as before. The lag equation alleviates the sensitivity to freestream turbulence levels that the 1998 version of the $k-\omega$ model is known to have. The formulation of the Lag model is computationally simple and requires less CPU time per iteration than the SA and SST models despite requiring the storage of an additional field variable. Information about the wall distance is not required for the Lag model as it is for the SA and SST models. The OVERFLOW implementation of the lag model requires 2^{nd} order upwind spatial discretizations to reduce numerical dissipation and grid density requirements. This turbulence model is still in the development stage and the present study is used to aid in the model verification and validation.

C. Grid Generation

All of the 2D grids were generated using the Chimera Grid Tools (CGT) package[30] and simple in-house grid generation codes. The 3D grids used in the end-effects study were generated with CGT and Gridgen. Double fringes were used in the overlap region interpolation stencils, and grids split simply for manual load balancing had 5 points of perfect overlap. Table 2 summarizes the number of grid points used in each case.

1. Compression ramps

The 2D compression ramp cases use a system similar to that depicted in Figure 1. The long flat plate region upstream of the corner is used to develop a turbulent boundary layer that matches the momentum thickness of the experimentally provided inflow profile. The OVERFLOW cases are run fully turbulent, so the length of this plate must be adjusted for each case to match the experimental momentum thickness. The corner and ramp regions are defined by three grids: two high resolution near-wall grids (split for load-balancing on multiple processors) and a grid in the freestream above the shock wave. It was found that the hyperbolic tangent stretching function used for the wall-normal direction did not place the desired number of grid points in the freestream above the shock wave, thus a separate zone was created. A low resolution sponge grid is used to contain the Mach wave generated at the upstream boundary (the 'sponge grid' terminology may be misleading here as the goal is not to use extreme grid stretching to attenuate disturbances, but rather to cheaply move the freestream boundary away from the region of interest). The final grid zone is used to better resolve the shock wave generated in the corner. The details of this grid can be found in reference[8,9] (it has little effect on the results presented in this paper).

The 3D compression ramp grids use a topology illustrated in Figure 2. The long region upstream of the corner generates the turbulent boundary layer, just as in the 2D case, except that it also generates boundary layers on the tunnel side walls (to simplify the problem, it is assumed that the side-wall boundary layers are the same thickness as on the tunnel floor). The tunnel floor and side-walls are resolved with a single high-resolution grid, and the 'freestream' flow in the middle of the tunnel uses a simple box grid.

All of the 2D Princeton cases use a wall spacing of $3.69 \cdot 10^{-5}$ in. ($3.9 \cdot 10^{-5}$ in. actual) and the 2D Kuntz cases use a wall spacing of $4.79 \cdot 10^{-5}$ in. ($4.9 \cdot 10^{-5}$ in. actual). The tops of the compression ramps are included in the simulation so that the expansion fan will insulate the compression corner and ramp face from upstream influences due to the 0^{th} order extrapolation outflow boundary condition and for accuracy of the computations. The 3D ramp grids are adapted by a preliminary solution such that the wall spacing varies to provide a nearly constant value of $Re_{cell} = 1.0$.

2. Cone-Flares

The cone-flare cases use the single zone, axisymmetric grids illustrated in Figure 3. The radius of the cone tip is assumed sharp, and an inviscid feeder block is used to permit the shock wave to develop as it may. The outer boundary is loosely fit to the shock wave and the wall spacing is $1.0 \cdot 10^{-5}$ in. As with the compression corner cases, the flare 'top' (a cylindrical section at the end of the ramp) is included in the grid, although this geometric feature is not discussed in the literature (and probably was not present). The ramp length was determined based on maximum x-value shown in the data plots in reference.[24]

D. Boundary Conditions

The boundary conditions for the 2D compression corner grid systems are freestream (IBTYP=40) at the inflow boundary, characteristic freestream (IBTYP=47) on the boundary opposite the viscous wall, and extrapolation (IBTYP=30) at the outflow. The viscous wall is isothermal (IBTYP=7). These same conditions were used for the 3D grids, with the tunnel floor and side walls as viscous walls and the tunnel 'ceiling' freestream (ie: the tunnel ceiling was not modeled). The cone-flare cases use characteristic freestream (IBTYP=47) opposite the isothermal viscous wall (IBTYP=8). Freestream (IBTYP=40) is specified on the inflow plane, the inviscid feeder block uses the inviscid adiabatic wall (IBTYP=1), and the outflow boundary uses extrapolation (IBTYP=30).

IV. Numerical Solution

Each of the OVERFLOW solutions is initialized to freestream conditions and iterated on a sequence of progressively finer grids until the finest grid level is obtained. These grids are created internally in OVERFLOW by specifying a number of grid levels (three grid levels would be the original fine grid, a medium grid with every other grid point used, and a coarse grid with every fourth grid point used). For this study, it was found that three grid levels and between 500 and 1,000 iterations on the coarse and medium grid levels reliably started up the solutions. Multigrid sequencing was utilized to accelerate convergence for most of the cases. In order to rapidly obtain a high quality steady-state solution, the dissipation parameters

for the matrix dissipation scheme[26] are ramped down to their optimum level as the solution converges. For more information on this process, see Lillard et al.[4]

The 2D solutions are considered to be iteratively converged with the optimal dissipation settings when the residuals have dropped by more than three orders of magnitude and the skin friction at several representative locations has converged to at least four significant digits. Iterative convergence was typically attained within 45,000 - 60,000 iterations; however, this number could have been lower had the dissipation settings been ramped in a different manner. The 3D cases showed iterative convergence after approximately 15,000 iterations, using a slightly different scheme (with the same final dissipation parameter values).

The grid convergence analysis used for the present study are described in detail in reference.[9] To summarize, the skin friction is the primary measure of grid convergence, with the separation length also being considered for flows with significant separation. Qualitative analysis (comparing plots of skin friction for fine/coarse grids) was used throughout, and quantitative analysis was used where possible. The Richardson Extrapolation and the grid convergence index (GCI) of Roache[31] are used to determine a quantitative measure of grid convergence for each 2D/axisymmetric case.

The 3D cases have not undergone as rigorous an analysis, however a qualitative grid convergence analysis has been performed. The grid resolution was refined by a constant factor of 1.5 in all 3 dimensions for one case (the Kuntz 24°ramp using the SST turbulence model), and the only significant difference in the skin friction plots (Figure 4) appears to be a slight steepening of the skin friction curve near separation. The initial grid resolution was used for the results computed for the other cases as the refined grids used too much CPU time to compute.

The DPLR solutions presented in this paper have been generated using the lessons learned from the OVERFLOW grid convergence study, and have not yet undergone a rigorous grid convergence analysis as the OVERFLOW solutions have. A more thorough study with DPLR is presently underway.

V. Results

Results from the various test cases computed by OVERFLOW are presented in this section along with discussion of the results. Where possible, each case uses the same non-dimensionalizing reference values used in the literature describing the dataset. These values are tabulated in Table 3.

A. 2D Surface Pressure

Figures 5 and 6 show the surface pressure predicted by OVERFLOW for the 2D Princeton and Kuntz compression ramps. The Kuntz dataset shows a greater tendency to separate, a likely effect of the lower Reynolds number. In general, for the 8° and 16° ramps, only small differences exist between the three turbulence models. Note that the apparent shift in the experimental pressures on the Kuntz 8° ramp is present in the experimental data. This offset is present for all ramp angles and no effort was made to shift this data; it was used as reported (it is discussed by Kuntz in reference[17]). Differences between the models start to become apparent at 16°, and continue to grow as the ramp angle increases to 20° and 24°. The SST model consistently shows the largest upstream influence, and the SA model shows the least. The SA model consistently predicts the most rapid pressure recovery of the three models, and the SST model shows the slowest. The lag model shows a tendency to rapidly recover once it reattaches, however the late reattachment appears to result in pressure predictions bounded by the SA and SST solutions. It is interesting to note that as the ramp angle increases, no one model does the best job of representing the profile relative to the experimental data; for each ramp angle, the 'best' model changes.

The surface pressure distributions predicted on the cone-flare models are shown in Figure 8. As with the weak compression ramp interactions, the unseparated case (36° flare) shows only small differences between the three turbulence models. For the separated case, however, the SST model shows significantly larger upstream influence than the other two models, and appears to predict the upstream influence reasonably well for this ramp angle. The SST model also shows a significant overprediction of the peak heating on the flare. It is really interesting that the lag model mimics the SA model so closely for both geometries of this test case; the reason for this behavior is unknown.

Wilcox[29] claims that RANS models typically show too little upstream influence and too large a wall pressure in the separated region. This observation appears to hold for the OVERFLOW solutions of the shallow ramp angles; however, it tends to predict too much upstream influence for the steeper ramps. It also

appears that the OVERFLOW solutions predict relatively accurate plateau pressures, though the oversized separation bubbles at higher ramp angles do tend to result in an overprediction of the plateau pressure.

As a broad generalization of the OVERFLOW results, the computed pressure plateaus tend to show an overly steep rise in pressure near the separation point. One possible reason for this discrepancy is shock-unsteadiness. In the experiments, the separation shock foot was observed to be unsteady. This means that the measured surface pressure near the separation point was actually a time-average, which would 'round-off' the pressure rise due to the separation shock. The RANS models, by nature, cannot capture this unsteadiness and instead predict a single location for the separation shock foot and the resulting steep pressure rise.

Note that the drop in pressure at the right-hand side of most of the plots is evidence of the expansion fan at the top of the ramp. The computed surface pressure distribution for both 24° ramps appears to be influenced by this expansion fan, indicating the importance that the computed ramp height match the experimental geometry.

B. 2D Skin Friction & Heat Transfer

Figure 7 shows the skin friction predicted by OVERFLOW for the Princeton compression ramps. For all of the compression ramps and all of the turbulence models, the computed skin friction profile shows a larger separation region compared to the experimental data. For all cases, the SST model predicts the largest separation bubble and the SA model predicts the smallest. In the recovery region, the lag model shows the most rapid recovery, typically more rapid than measured. The SA model recovers too slowly for all ramp angles. The SST model prediction is interesting in that it predicts the correct trend in skin friction recovery for all four ramp angles; however, it appears that the late reattachment results in the computed skin friction being lower in magnitude than in the experiment.

Figure 9 shows the heat transfer of the Princeton 16° ramp. The heat transfer predictions show large variations between the three turbulence models. The SST model does a good job predicting the heat transfer early in the recovery, but drops below the heat transfer levels seen in the experiment towards the second-half of the ramp. The lag model overpredicts the increase in heat transfer near the corner, but also underpredicts the downstream levels. The SA model underpredicts the heat transfer along the entire length. It should be noted that the upstream heat transfer levels were not provided in reference,[20] so the relative accuracy of the zero-pressure gradient boundary layer heat transfer computations is not available for this dataset.

The heat transfer distributions on the cone-flares (Figure 10) show similar differences between the three turbulence models. For the unseparated case (36° flare), the SST and lag models appear to provide reasonable predictions of the heat transfer in the recovery region. The SA model, as before, does not show enough of a rise in heating. The same observation can be made for the separated case (42° flare); the SA model prediction does not appear to show a significant change in behavior due to the presence of separation. The SST model shows a significant overprediction of the peak heating, and the peak occurs farther downstream than observed. The delayed peak would seem to suggest late reattachment, however the SST model shows a (surprisingly) good prediction of the heating in the separation region. The lag model recovery is too rapid, but it does a better job at estimating the peak heating rate.

Wilcox[29] states that RANS models typically overpredict C_f and C_h downstream of a shock-boundary layer interaction. The computed results in the present study seem to show a general trend to underpredict the skin friction in the recovering boundary layer for flows with significant separation, although the lag model does occasionally show larger skin friction than the experiment. It is likely, however, that this underprediction is due primarily to the oversized separation bubble and the corresponding late reattachment point, as the 8° ramp (with only minor separation) shows too rapid a recovery for all three turbulence models. The heat transfer results in this study do not really support or discredit Wilcox's claim as the differences between each of the models straddles the experimental data.

The results presented by Sinha[32] tell pretty much the same story as the results in this document. He found that the SA model underpredicted both the peak heating and pressure, and did not really show much of a peak. Neither of his computations show signs of separation.

C. Comparison to DPLR

Figure 11 shows the comparison of the OVERFLOW solutions and the DPLR solutions for the Princeton 8° and 24° ramps. The DPLR and OVERFLOW implementations of the SA and SST turbulence model shows slight differences in the prediction of the undisturbed boundary layer. They show identical trends in

the separation behavior for these two turbulence models, with DPLR showing a larger separation for the SST model than OVERFLOW predicts.

D. 3D End Effects

Figure 12 shows the effect of adding the side-wall boundary layers to the compression corner shock boundary layer interaction. The pseudo-surface streak lines show slightly curved separation and reattachment lines, and indicate a very complex flow pattern near the walls. The red streamlines near the centerline show an escape path for the flow trapped in the recirculating separation bubble. This would seem to imply that the separation bubble could be smaller in this case than for a strictly 2D flow. Figure 13 shows the skin friction on the centerline of the 3D runs compared to the 2D computations for each turbulence model. The end-effects do indeed cause the separation point to move closer to the corner for all three turbulence models, improving the prediction for each model. The reattachment prediction improves for the lag model, remains the same for the SST model, and actually gets worse for the SA model. The surface pressures shown in Figure 14 show similar improvements, with a rather remarkable improvement in the prediction by the lag model. Clearly for this test case, the three-dimensional end-effects cannot be neglected. Present efforts are directed at performing 3D computations for the Princeton dataset.

E. SWBLI Discussion

Knight et al.[33] states that RANS computations for compression corner shock boundary layer interactions are accurate for weak interactions, but significant discrepancies existed for strong interactions. While it is difficult to define the dividing line between 'weak' and 'strong' interactions, the present results seem to agree with this assessment. The 8° ramp results tend to be reasonably accurate, but the accuracy decreases as the interactions are strengthened.

Knight et al.[33] places a strong emphasis on the fact that the RANS computations fail to predict the low-frequency shock unsteadiness;[34] the OVERFLOW solutions likewise do not predict any unsteadiness. This should be expected, however, as recent findings[35] suggest that the low frequency oscillations are the result of large streamwise turbulent structures in the upstream boundary layer. Since the RANS models average out all of the turbulent fluctuations, including these large streamwise features, there is no physical source for this type of shock unsteadiness. In preliminary computations, the shock waves did occasionally show an oscillatory motion of the shock foot location that prevented convergence to a steady solution; however, efforts to run these solutions time-accurate failed to produce consistent and repeatable results. This 'unsteadiness' was considered to be a numerical problem and was fixed by reducing the grid aspect ratio near separation and by increasing the CFL number.

One more thing is interesting to note about the presented results. On the Princeton 16° ramp, Figure 5(b) shows a rather accurate prediction of the surface pressure, but Figure 9 shows a very poor heat transfer prediction. This shows that the code can accurately predict the inviscid flow field (and hence, gets the inviscid pressure correct), but still get the viscous boundary layer wrong. Assessing the accuracy of a CFD simulation using pressure only does not indicate anything about the accuracy of skin friction or heating prediction.

Finally, it has been shown that the 2D assumption is indeed a questionable one for plane compression ramp flows. It is helpful to note, however, that knowledge of the exact geometry run can help reconcile the difference as far as model validation is concerned.

Acknowledgments

This work is supported by the NASA Johnson Space Center under Grant No. NNJ04HI12G. We would also like to thank Tom Gatski for providing information on his DNS simulations, Dave Kuntz and Lex Smits for providing us with documents and information on each of their experiments.

References

[1]Jespersen, D. C., Pulliam, T. H., and Buning, P. G., "Recent Enhancements to OVERFLOW," AIAA Paper No. 97-0644, January 1997.

[2]Buning, P., Jespersen, D., Pulliam, T., Klopfer, G., Chan, W., Slotnick, J., Krist, S., and Renze, K., *OVERFLOW User's Manual, Version 1.8s*, NASA Langley Research Center, 2000.

[3]Olsen, M. E. and Prabhu, D. K., "Application of OVERFLOW to Hypersonic Perfect Gas Flowfields," AIAA Paper No. 2001-2664, June 2001.

[4]Lillard, R. P. and Dries, K. M., "Laminar Heating Validation of the OVERFLOW Code," AIAA Paper No. 2005-0689, January 2005.

[5]Spalart, P. R. and Allmaras, S. R., "A One-Equation Turbulence Model for Aerodynamic Flows," AIAA Paper No. 92-0439, January 1992.

[6]Menter, F., Grotjans, H., and Unger, F., "Numerical Aspects of Turbulence Modeling for the Reynolds Averaged Navier-Stokes Equations," VKI Lecture Series, March 1997, pp. 1–45.

[7]Olsen, M. E. and Coakley, T. J., "The Lag Model, a Turbulence Model for Non-Equilibrium Flows," AIAA Paper No. 2001-2564, June 2001.

[8]Oliver, A. B., Lillard, R. P., Blaisdell, G. A., and Lyrintzis, A. S., "Validation of High-Speed Turbulent Boundary Layer and Shock-Boundary Layer Interaction Computations With the OVERFLOW Code," AIAA Paper No. 2006-0894, January 2006.

[9]Oliver, A. B., *Evaluation of Two-Dimensional High-Speed Turbulent Boundary Layer and Shock-Boundary Layer Interaction Computations With the OVERFLOW Code*, MS Thesis, Purdue University, West Lafayette, IN, August 2006.

[10]Cary, A. M., *Turbulent Boundary Layer Heat Transfer and Transition Measurements With Extreme Surface Cooling in Hypersonic Flows*, MS Thesis, University of Virginia, Charlottesville, VA, August 1969.

[11]Gatski, T. B. and Erlebacher, G., "Numerical Sumulation of a Spatially Evolving Supersonic Turbulent Boundary Layer," Tech. Rep. NASA TM 211934, NASA Langley Research Center, Hampton, VA, September 2002.

[12]Pirozzoli, S., Grasso, F., and Gatski, T. B., "Direct Numerical Simulation and Analysis of a Spatially Evolving Supersonic Turbulent Boundary Layer at M=2.25," *Physics of Fluids*, Vol. 16, No. 3, March 2004, pp. 530–545.

[13]Settles, G. S., Fitzpatrick, T. J., and Bogdonoff, S. M., "Detailed Study of Attached and Separated Compression Corner Flowfields in High Reynolds Number Supersonic Flow," *AIAA Journal*, Vol. 17, No. 6, June 1979, pp. 579–585.

[14]Smits, A. and Muck, K., "Experimental Study of Three Shock Wave/Turbulent Boundary Layer Interactions," *Journal of Fluid Mechanics*, Vol. 182, Sept. 1987, pp. 291–314.

[15]Kuntz, D., Amatucci, V. A., and Addy, A. L., "Turbulent Boundary-Layer Properties Downstream of the Shock-Wave/Boundary-Layer Interaction," *AIAA Journal*, Vol. 25, May 1987, pp. 668–675.

[16]Kuntz, D., Amatucci, V. A., and Addy, A. L., "The Turbulent Boundary Layer Properties Downstream of the Shock-Wave/Boundary-Layer Interaction," AIAA Paper No. 86-0348, 1986.

[17]Kuntz, D., *An Experimental Investigation of the Shock Wave-Turbulent Boundary Layer Interaction*, PhD Thesis, University of Illinois, Urbana-Champaign, IL, May 1985.

[18]Settles, G. S. and Dodson, L. J., "Hypersonic Shock/Boundary-Layer Interaction Database: New and Corrected Data," Tech. Rep. 177638, Pennsylvania State University, University Park, PA, April 1994, NASA Contractor Report.

[19]Settles, G. S. and Dodson, L. J., "Hypersonic Shock/Boundary-Layer Interaction Database," Tech. Rep. 177577, Pennsylvania State University, University Park, PA, April 1991, NASA Contractor Report.

[20]Evans, T. T. and Smits, A. J., "Measurements of the Mean Heat Transfer in a Shock Wave - Turbulent Boundary Layer Interaction," *Experimental Thermal and Fluid Science*, , No. 12, 1996, pp. 87–97.

[21]Kline, S. J., editor, *The 1980-81 AFOSR-HTTM-Stanford conference on complex turbulent flows: Comparison of computation and experiment*, Feb. 1981.

[22]Kuntz, D. W., Private Communication.

[23]Maise, G. and McDonald, H., "Mixing Length and Kinematic Eddy Viscosity in a Compressible Boundary Layer," *AIAA Journal*, Vol. 6, No. 1, January 1968, pp. 73–80.

[24]Holden, M., "Studies of the Mean and Unsteady Structure of Turbulent Boundary Layer Separation in Hypersonic Flow," AIAA Paper No. 91-1778, June 1991.

[25]Chan, W. M., Gomez, R. J., Rogers, S. E., and Buning, P. G., "Best Practices in Overset Grid Generation," AIAA Paper No. 2002-3191, June 2002.

[26]Swanson, R. and Turkel, E., "On Central-Difference and Upwind Schemes," Tech. Rep. 182061, NASA Langley Research Center, Hampton, VA, June 1993, NASA Contractor Report (ICASE).

[27]Paciorri, R., Dieudonne, W., Degrez, G., Charbonnier, J.-M., and Deconinck, H., "Validation of the Spalart-Allmaras turbulence model for application in hypersonic flows," AIAA Paper No. 1997-2023, June 1997.

[28]Olsen, M. E., Lillard, R. P., and Coakley, T. J., "The Lag Model Applied to High Speed Flows," AIAA Paper No. 2005-0101, January 2005.

[29]Wilcox, D. C., *Turbulence Modelling for CFD*, DCW Industries, La Canada, CA, 2002.

[30]Chan, W., Rogers, S., Nash, S., Buning, P., and Meakin, R., "User's Manual for Chimera Grid Tools," On the WWW, September 2004, `URL http://people.nas.nasa.gov/ rogers/cgt/doc/man.html`.

[31]Roache, P. J., "Perspective: A Method for Uniform Reporting of Grid Refinement Studies," *Journal of Fluids Engineering*, Vol. 116, No. 3, 1994, pp. 405–413.

[32]Sinha, K., "Shock Unsteadiness Model Applied to Hypersonic Shock-Wave/Turbulent Boundary Layer Interactions," AIAA Paper No. 2006-0126, January 2006.

[33]Knight, D., Yan, H., Panaras, A. G., and Zheltovodov, A., "Advances in CFD Prediction of Shock Wave Turbulent Boundary Layer Interactions," *Progress in Aerospace Sciences*, Vol. 39, 2003, pp. 121–184.

[34]Dolling, D. S., "50 Years of Shock Wave/Boundary Layer Interaction - What Next?" AIAA Paper No. 2000-2596, June 2000.

[35]Ganapathisubramani, B., Clemens, N., and Dolling, D., "Planar imaging measurements to study the effect of spanwise structure of upstream turbulent boundary layer on shock induced separation," AIAA Paper No. 2006-0324, January 2006.

Table 1. Freestream and inflow boundary layer data for compression ramp cases

Princeton Ramps	8°	16°	20°	24°
M_∞	2.87	2.85	2.85	2.84
T_0 [K]	280	268	258	262
P_0 [Pa]	6.90E+05	6.90E+05	6.90E+05	6.90E+05
δ [mm]	26	26	25	23
δ^* [mm]	6.7	6.3	6.6	6.1
θ [mm]	1.3	1.3	1.3	1.2
$x_{upstream}$ [mm]	-50.8	-50.8	-50.8	-50.8
Re_∞ $[m^{-1}]$	$60.8 \cdot 10^6$	$65.6 \cdot 10^6$	$69.5 \cdot 10^6$	$68.3 \cdot 10^6$
Re_δ	$1.58 \cdot 10^6$	$1.71 \cdot 10^6$	$1.74 \cdot 10^6$	$1.57 \cdot 10^6$

Kuntz Ramps	8°	16°	20°	24°
M_∞	2.94	2.94	2.94	2.94
T_0 [K]	294.15	303.15	303.15	302.15
P_0 [Pa]	4.83E+05	4.83E+05	4.83E+05	4.83E+05
δ [mm]	8.27	8.27	8.27	8.27
δ^* [mm]	3.11	3.11	3.11	3.11
θ [mm]	0.574	0.574	0.574	0.574
$x_{upstream}$ [mm]	0.0	0.0	0.0	0.0
Re_∞ $[m^{-1}]$	$38.1 \cdot 10^6$	$36.4 \cdot 10^6$	$36.4 \cdot 10^6$	$36.6 \cdot 10^6$
Re_δ	$0.315 \cdot 10^6$	$0.301 \cdot 10^6$	$0.301 \cdot 10^6$	$0.302 \cdot 10^6$

Table 2. Grid dimensions used in presented computations

Grid	Zone						Total Points
	1	2	3	4	5	6	
Kuntz 8°	172x227	220x181	85x181	300x53	221x39	120x24	121.6E+3
Kuntz 16°	172x227	216x181	41x181	252x53	221x39	75x24	109.3E+3
Kuntz 20°	172x227	216x181	48x181	259x53	221x39	30x24	109.9E+3
Kuntz 24°	72x227	216x181	48x181	259x53	221x39	-	109.2E+3
Princeton 8°	123x167	182x144	181x144	358x28	250x39	120x24	95.5E+3
Princeton 16°	123x167	180x144	180x144	355x28	240x39	120x24	94.6E+3
Princeton 20°	153x208	177x144	130x144	302x35	221x39	45x19	96.1E+3
Princeton 24°	153x208	176x144	155x144	326x35	221x39	-	99.5E+3
Cone-Flare 36°	1452x363	-	-	-	-	-	527.1E+3
Cone-Flare 42°	1451x363	-	-	-	-	-	526.7E+3

Table 3. Reference values used in data reduction

Case	δ_{Ref} [m]	M_{Ref}	V_{Ref} [m/s]	P_{Ref} [Pa]	ρ_{Ref} $[kg/m^3]$
Princeton Ramps:					
8°	0.026	2.87	591.5	22856	-
16°	0.026	2.85	577.2	23561	-
20°	0.025	2.85	566.3	23561	-
24°	0.023	2.84	569.9	23922	-
Kuntz Ramps:					
8°	0.00827	2.94	611.8	14391	-
16°	0.00827	2.94	621.0	14391	-
20°	0.00827	2.94	621.0	14391	-
24°	0.00827	2.94	620.0	14391	-
Cone-Flares:					
36°	0.01778	10.96	1805	-	0.0327
42°	0.01778	10.96	1805	-	0.0327

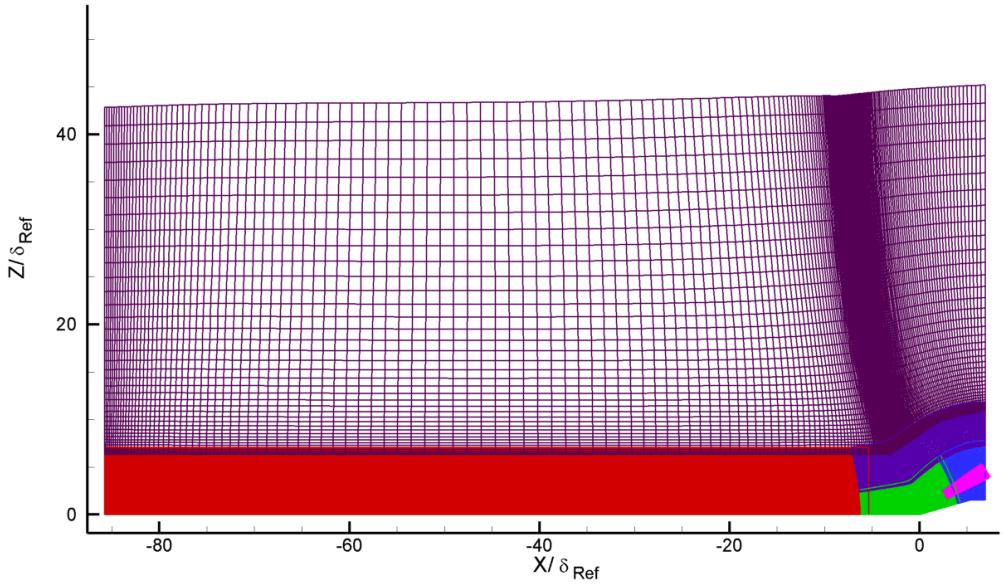

(a)

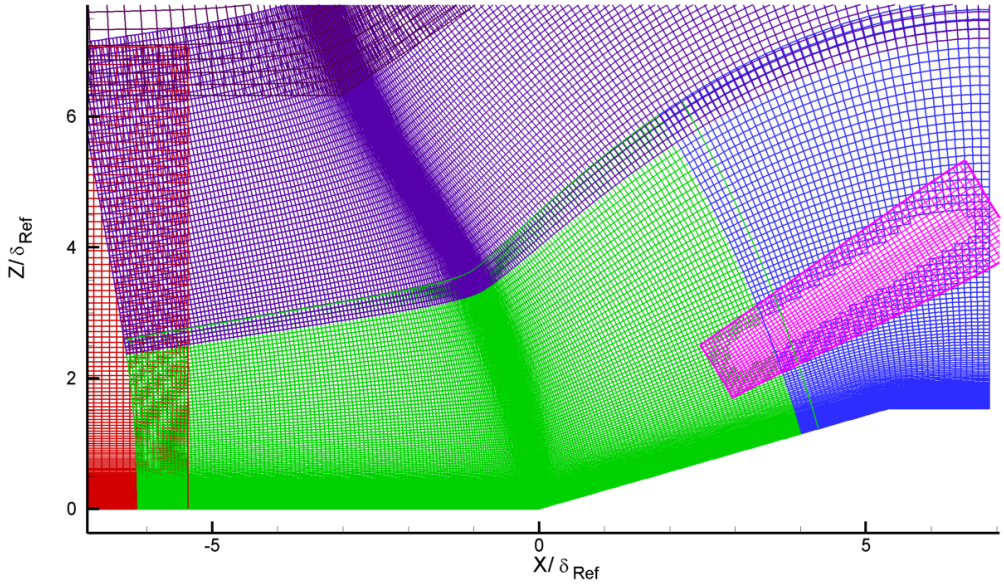

(b)

Figure 1. General grid topology for the 2D compression ramp cases. (a) Entire domain, (b) Detail of corner region.

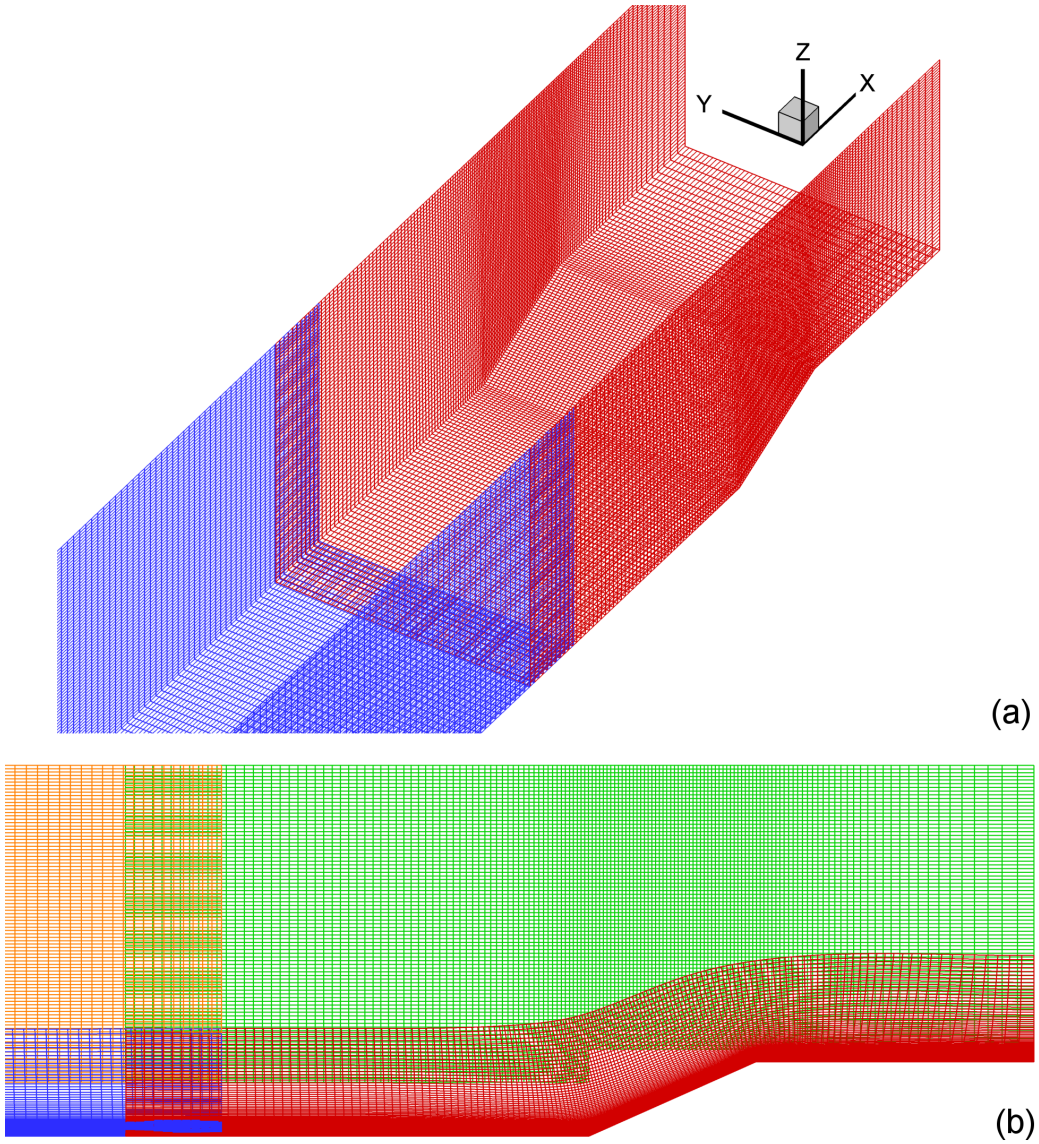

Figure 2. General grid topology for the 3D compression ramp cases. (a) Surface grids, (b) Centerline cross-section of grid system.

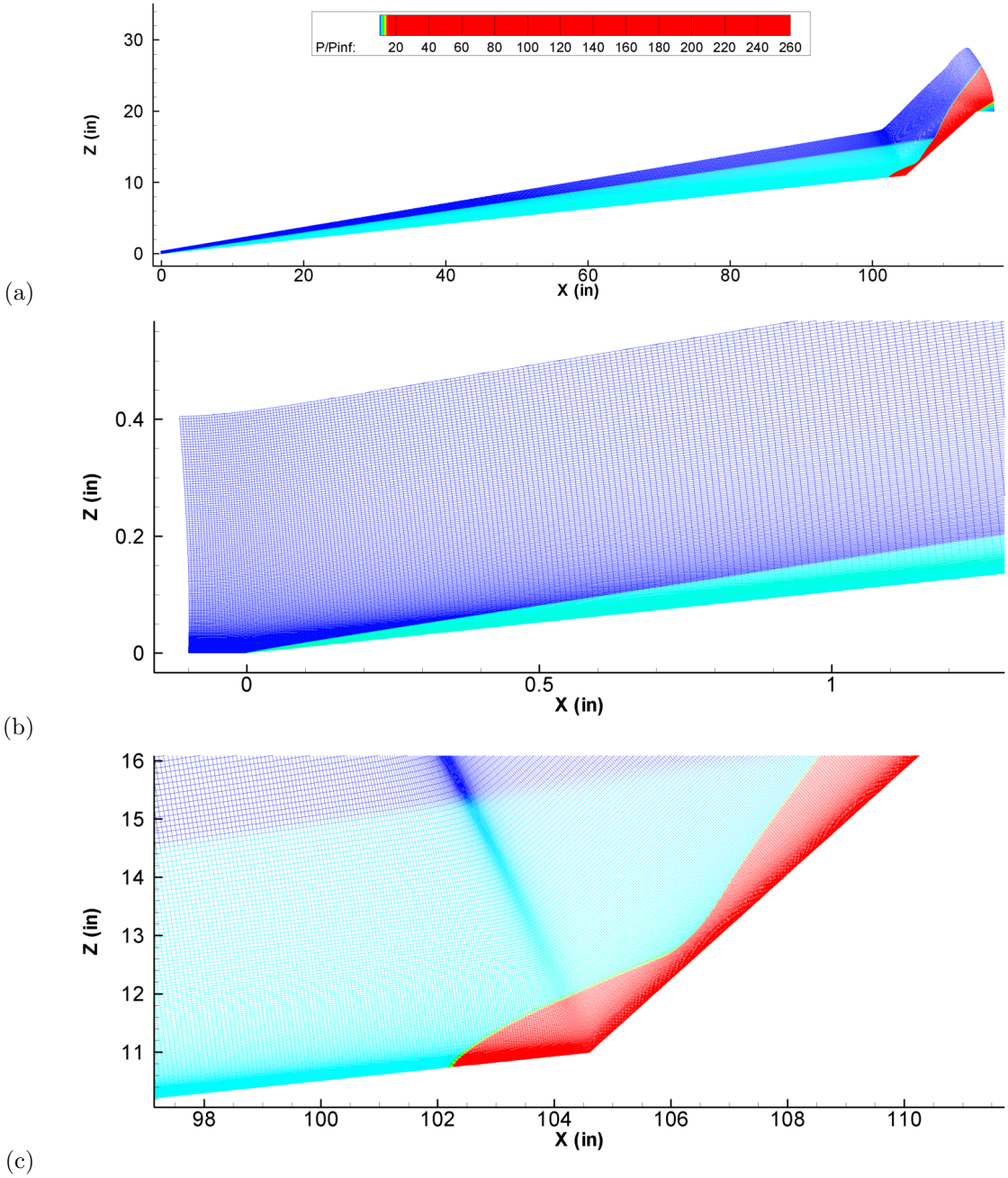

Figure 3. General grid topology for the cone-flare cases. (a) Entire domain, (b) Detail of tip region, (c) Detail of corner region, colored by static pressure (color scale adjusted to show shock locations).

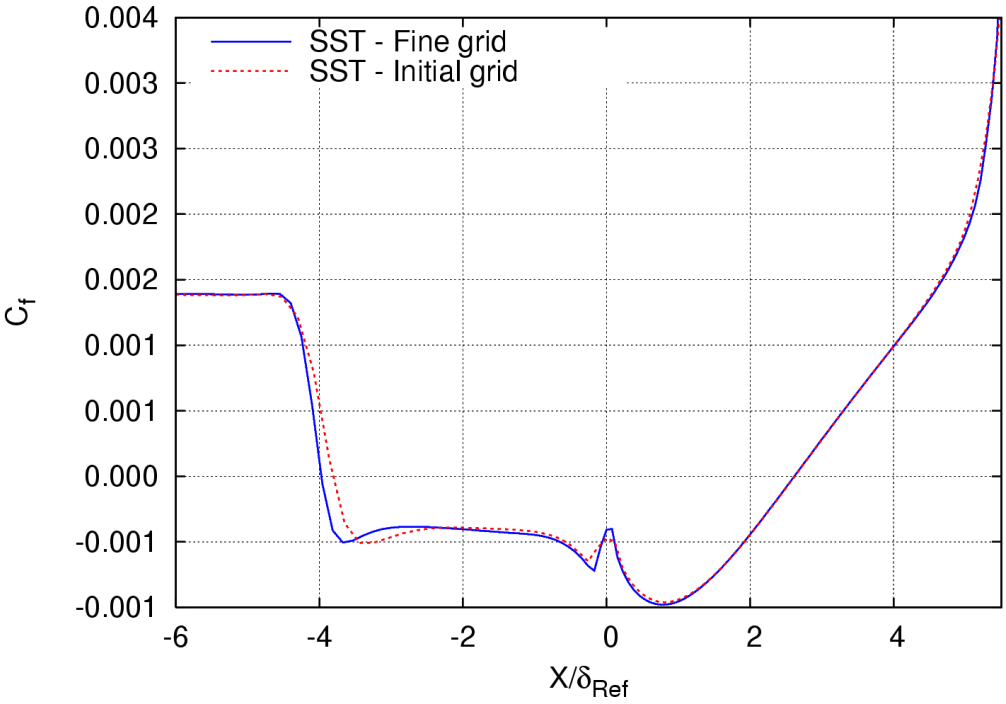

Figure 4. Grid sensitivity of skin friction distribution along centerline of Kuntz 24° ramp.

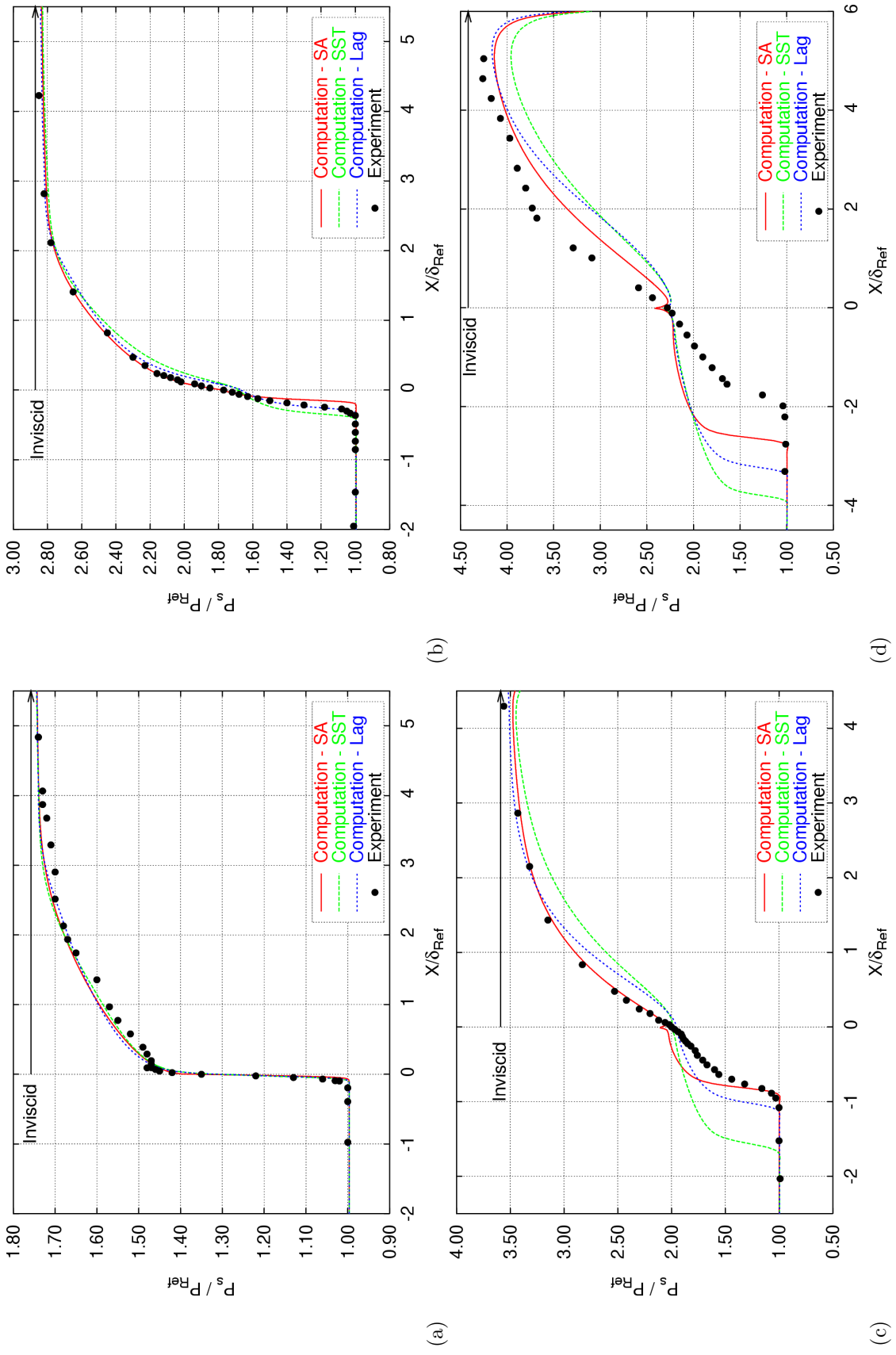

Figure 5. Surface pressure distributions for Princeton series. (a) 8° ramp, (b) 16° ramp, (c) 20° ramp, (d) 24° ramp.

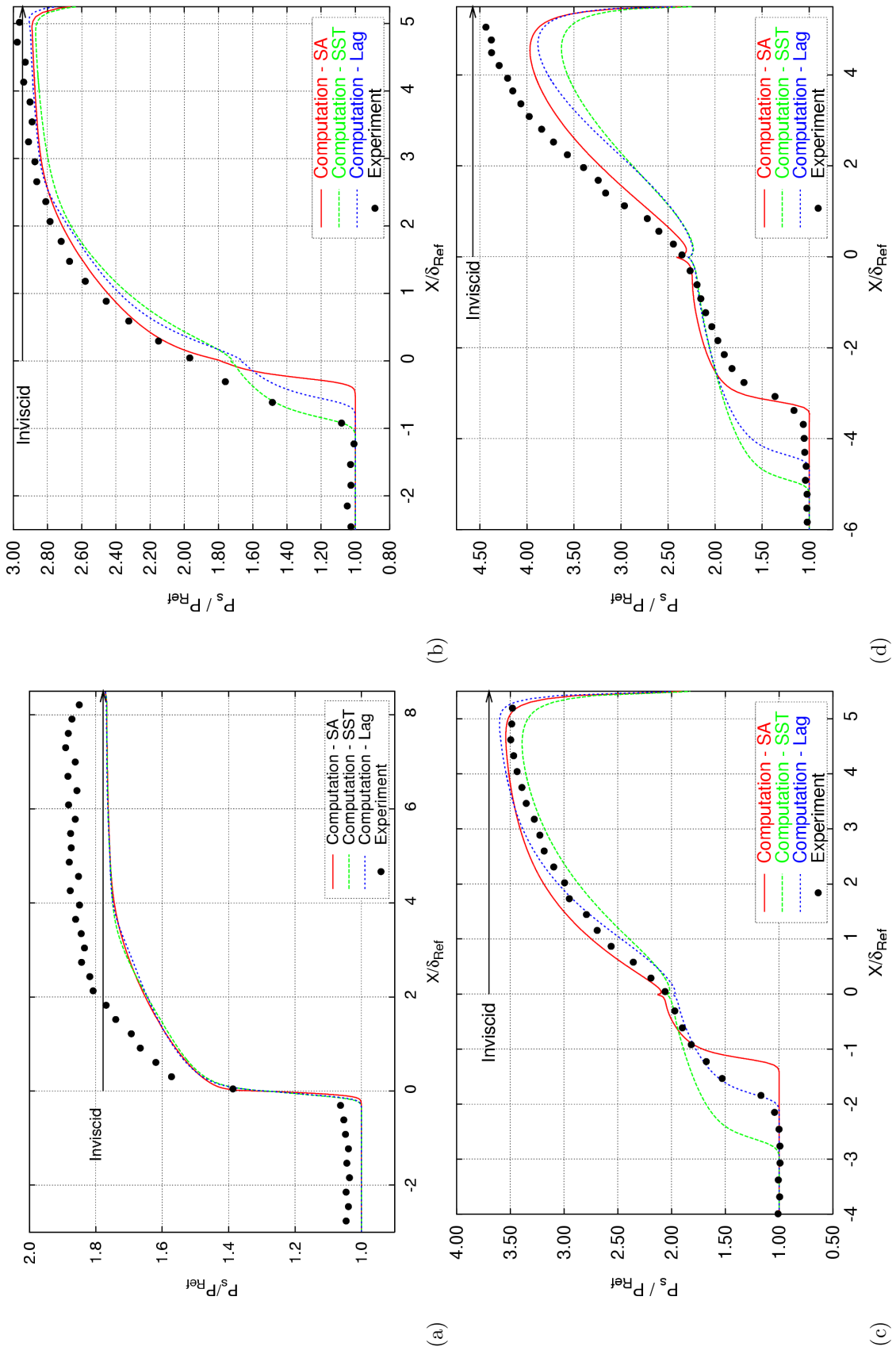

Figure 6. Surface pressure distributions for Kuntz series. (a) 8° ramp, (b) 16° ramp, (c) 20° ramp, (d) 24° ramp.

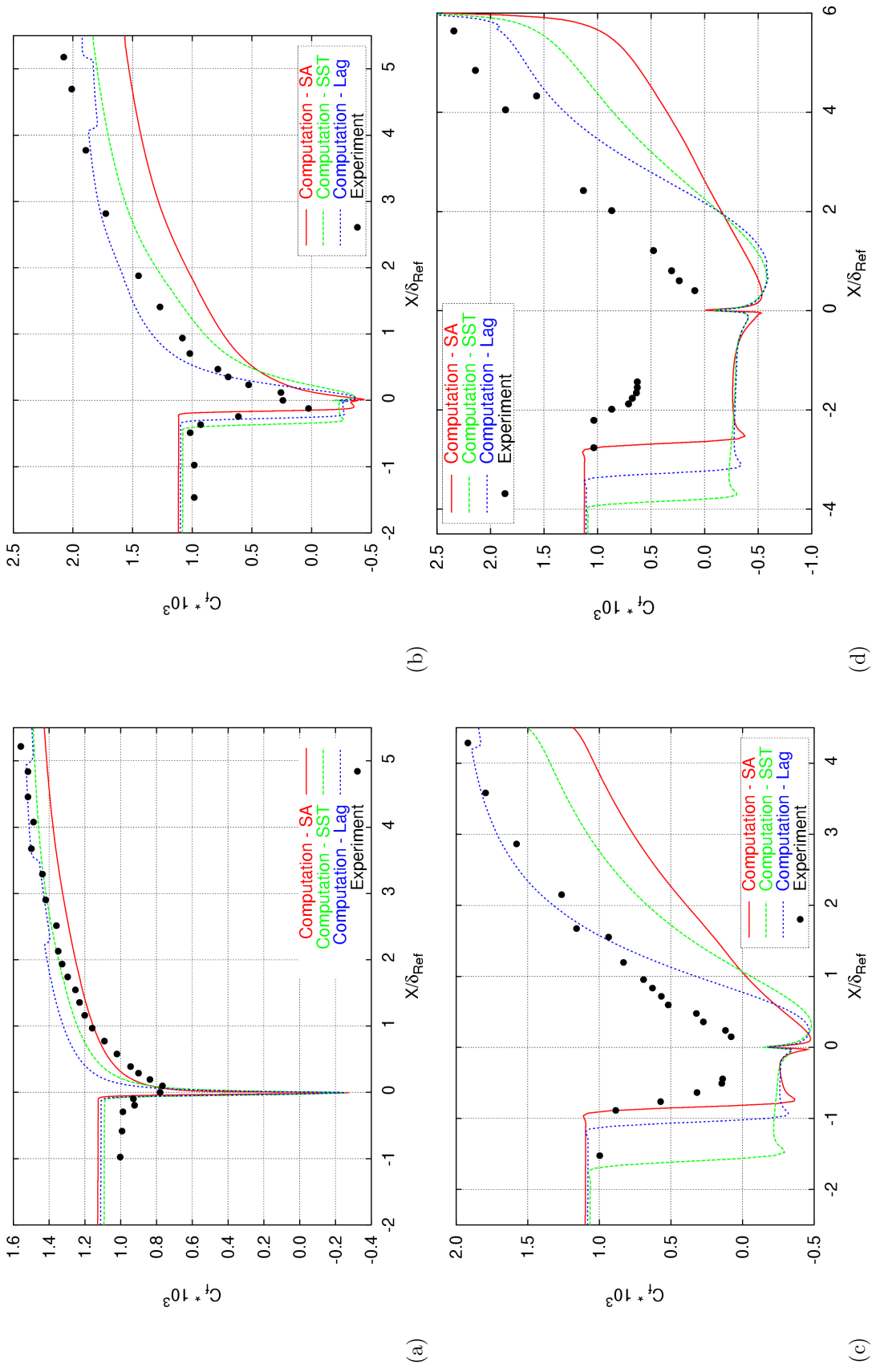

Figure 7. Skin friction distribution for Princeton series. (a) 8° ramp, (b) 16° ramp, (c) 20° ramp, (d) 24° ramp.

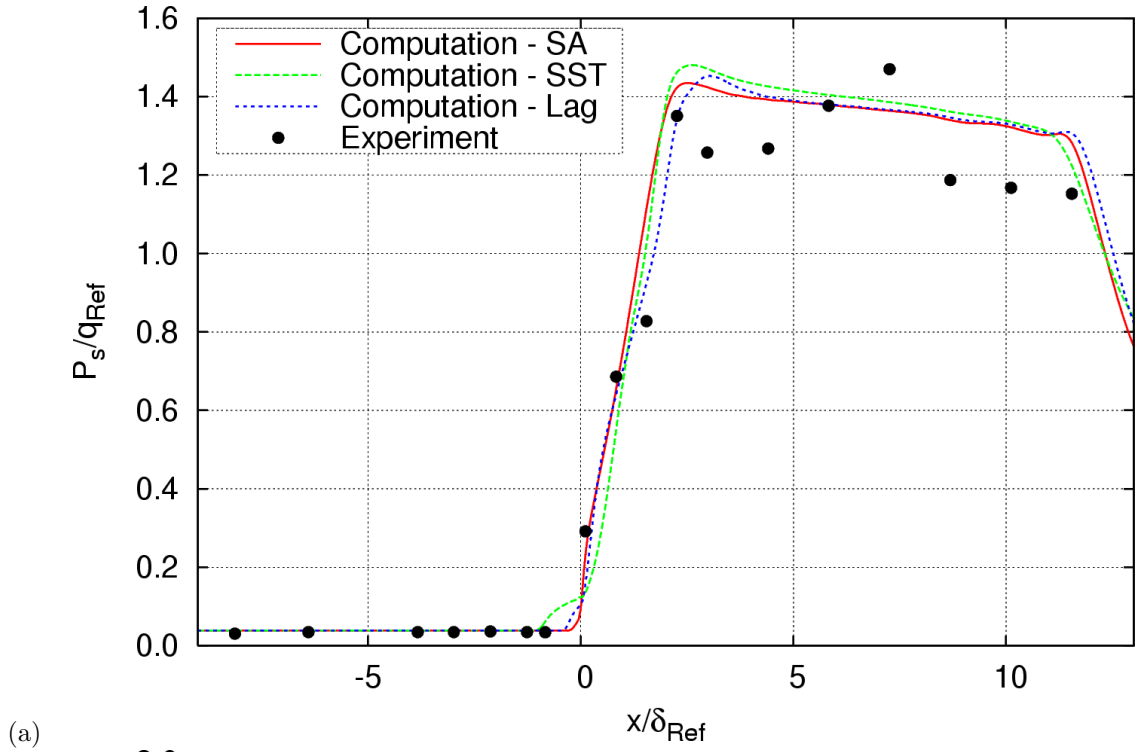

(a)

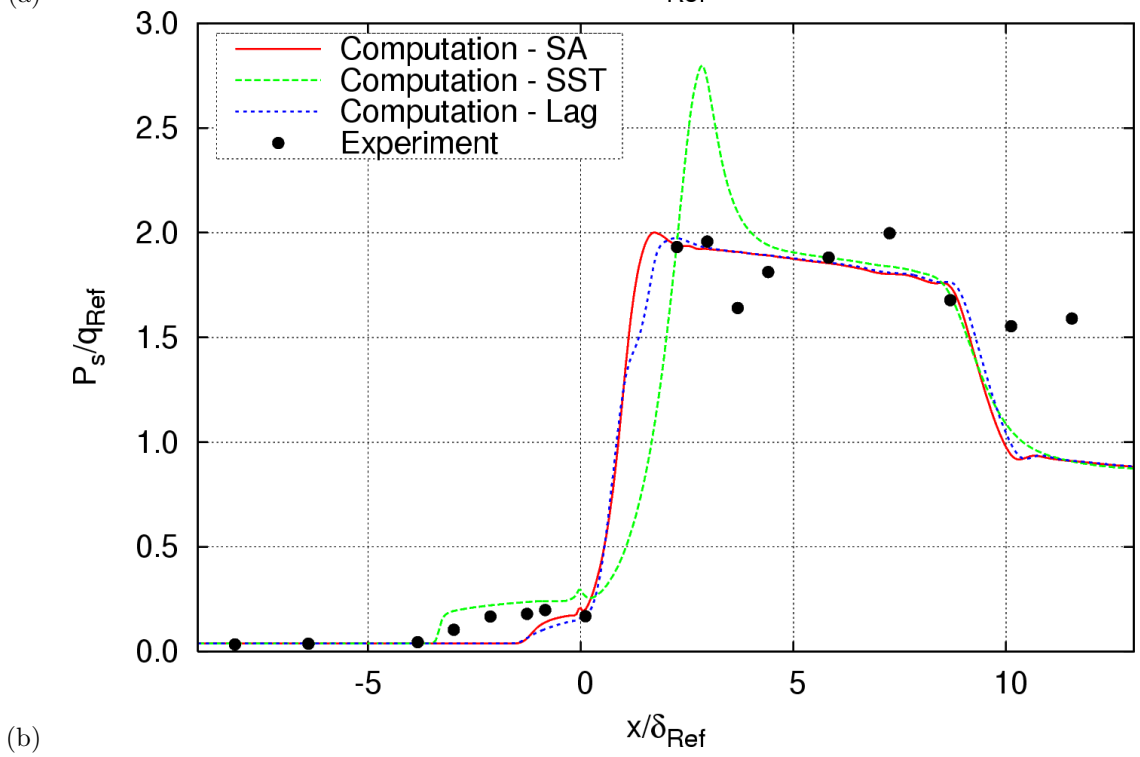

(b)

Figure 8. Surface pressure distribution on cone-flares. (a) 36° flare, (b) 42° flare.

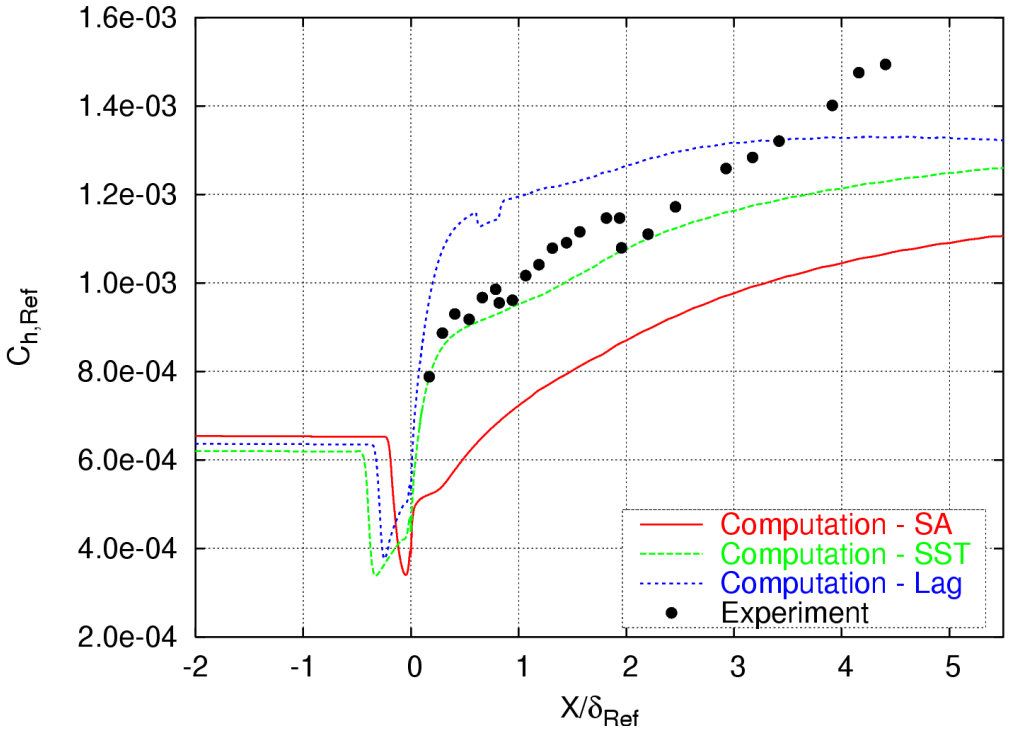

Figure 9. Heat transfer distribution for Princeton 16° ramp.

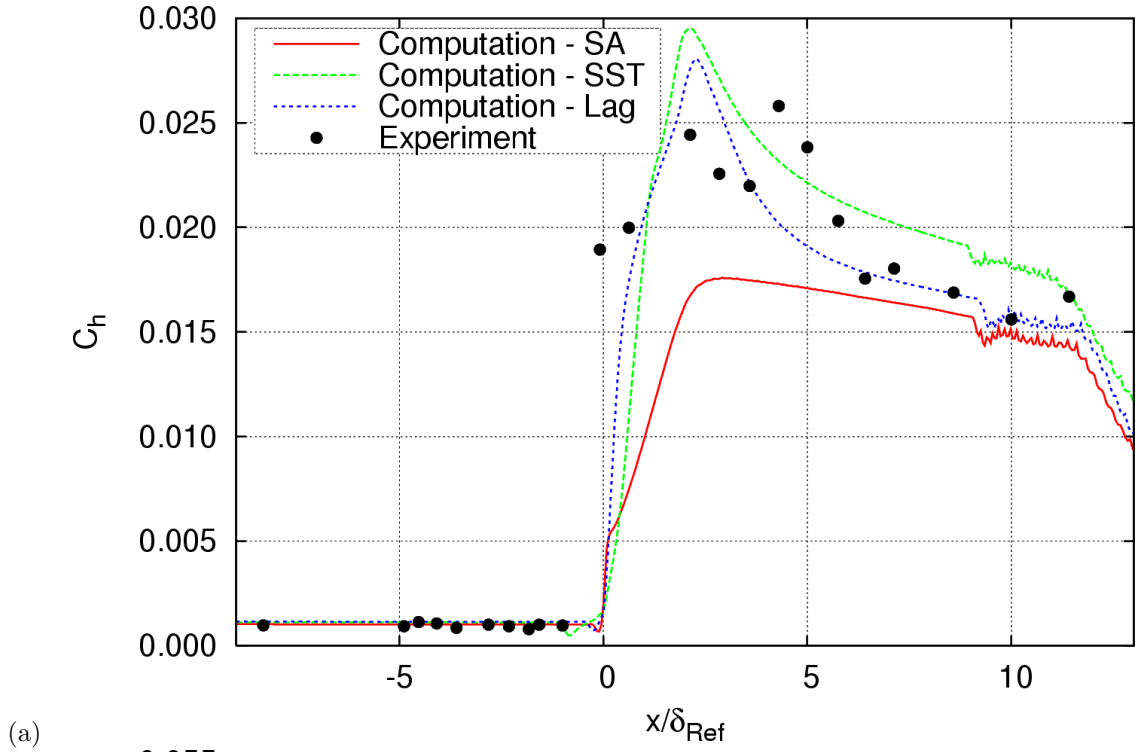

(a)

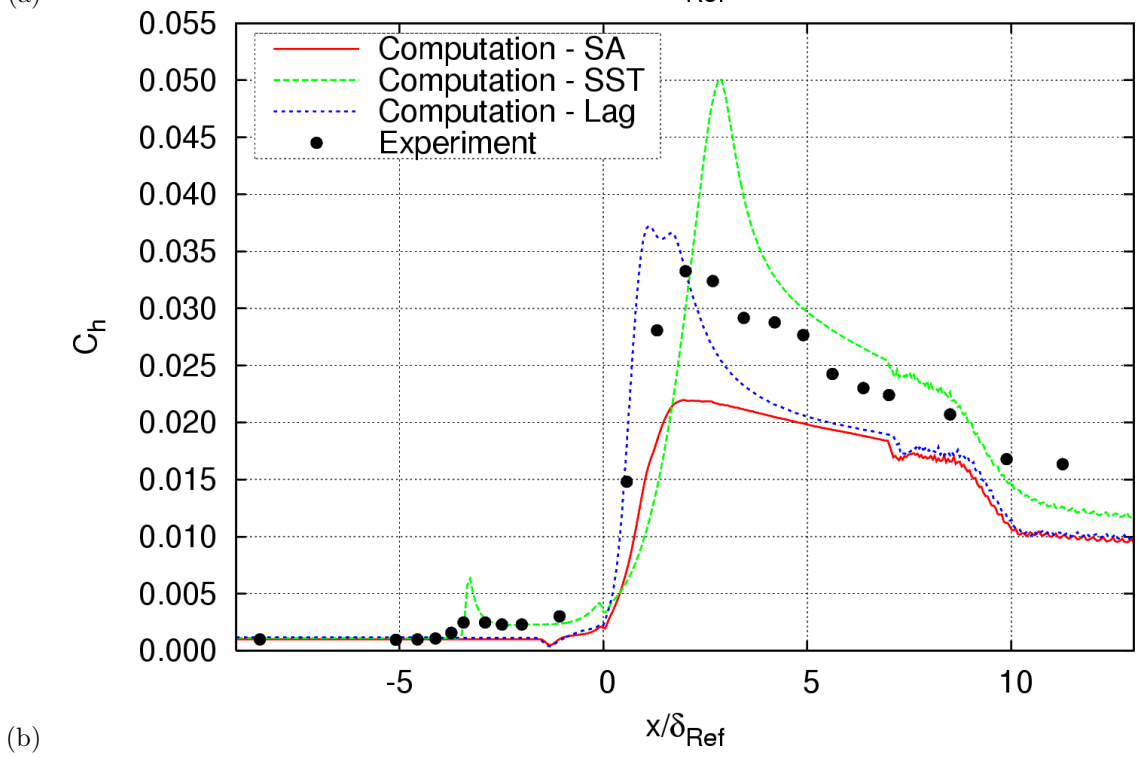

(b)

Figure 10. Heat transfer distribution on cone-flares. (a) 36° flare, (b) 42° flare.

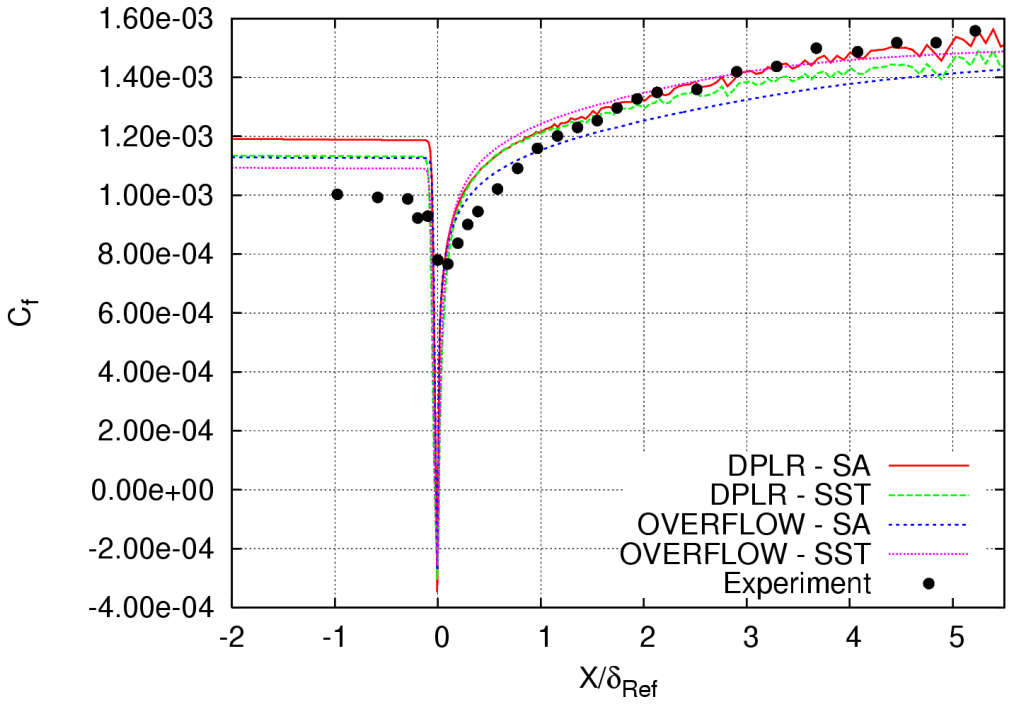

(a)

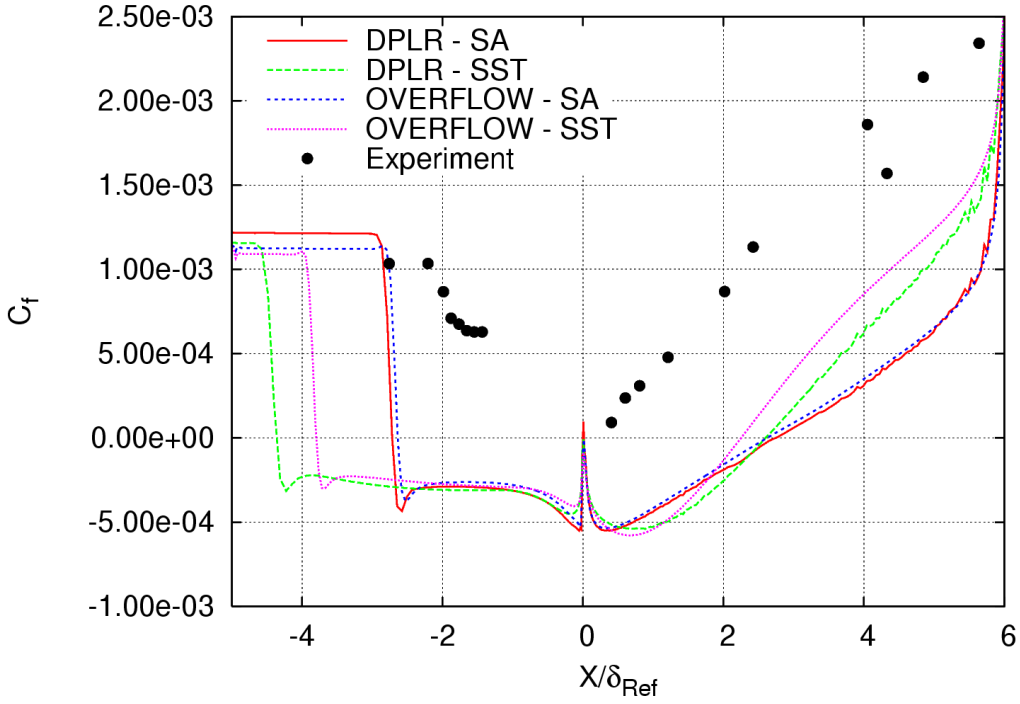

(b)

Figure 11. Skin friction predicted by DPLR of (a) Princeton 8° ramp, (b) Princeton 24° ramp.

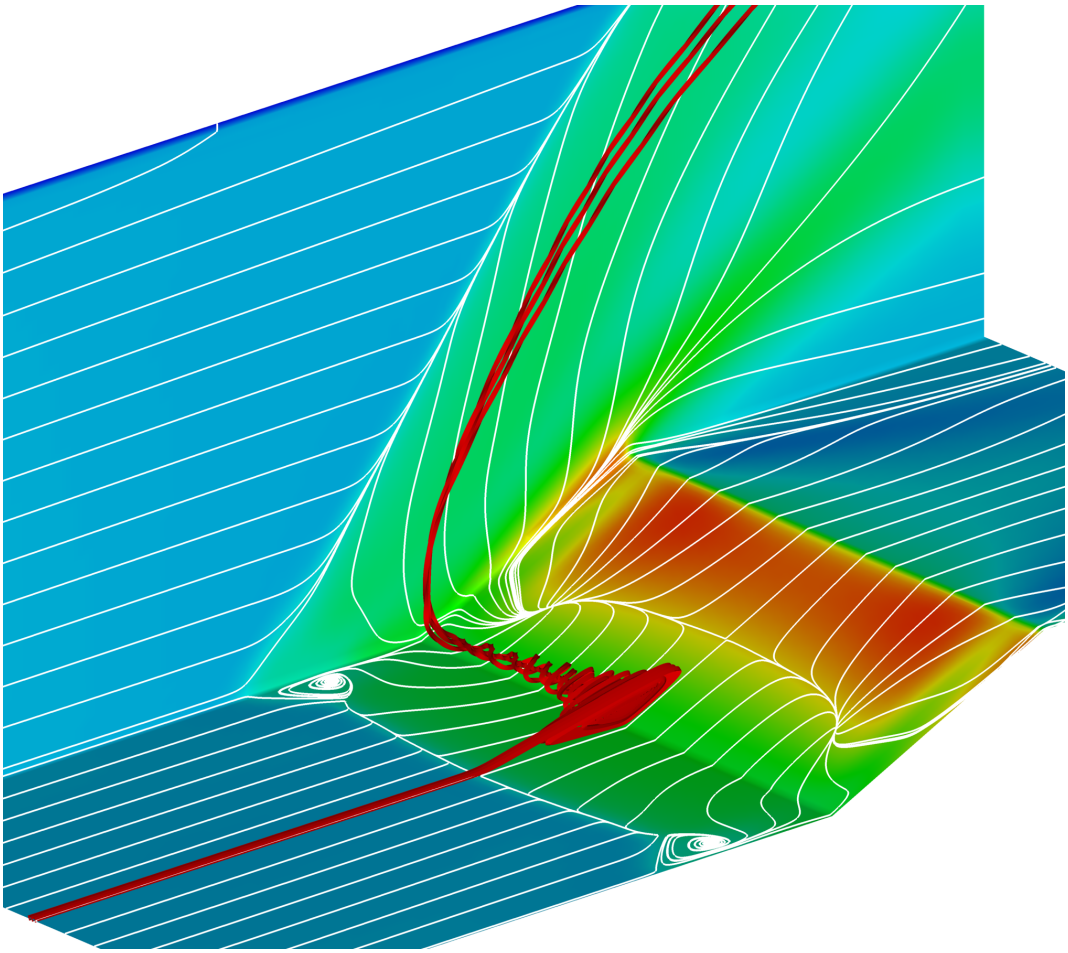

Figure 12. Surface streaks and pressure contours on Kuntz 24° ramp.

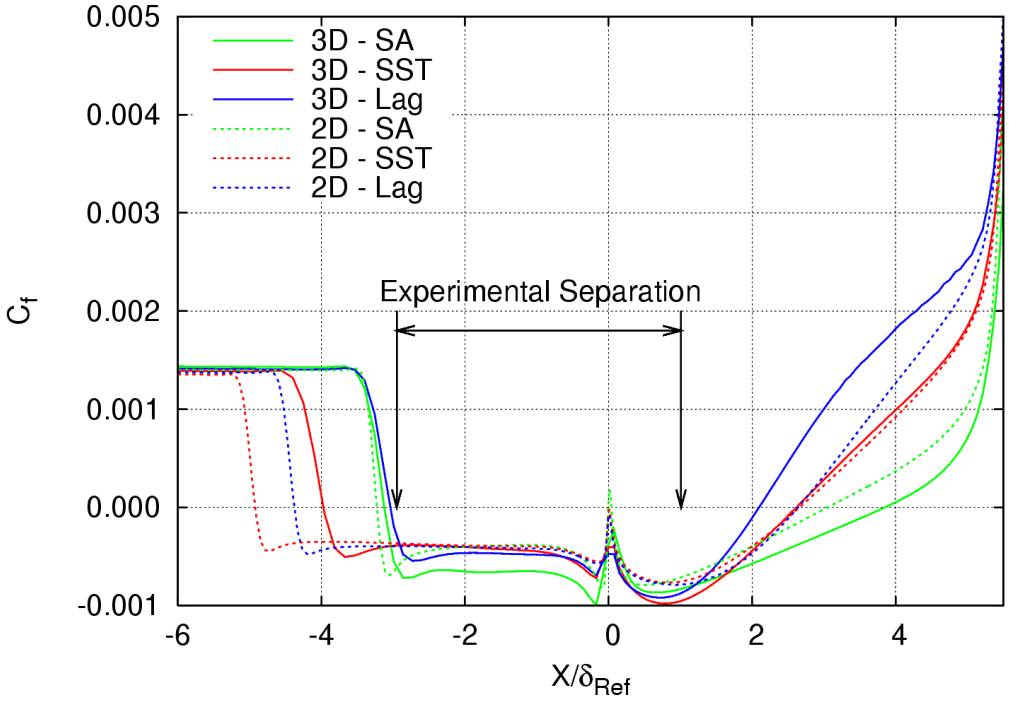

Figure 13. Skin friction distribution along centerline of Kuntz 24° ramp.

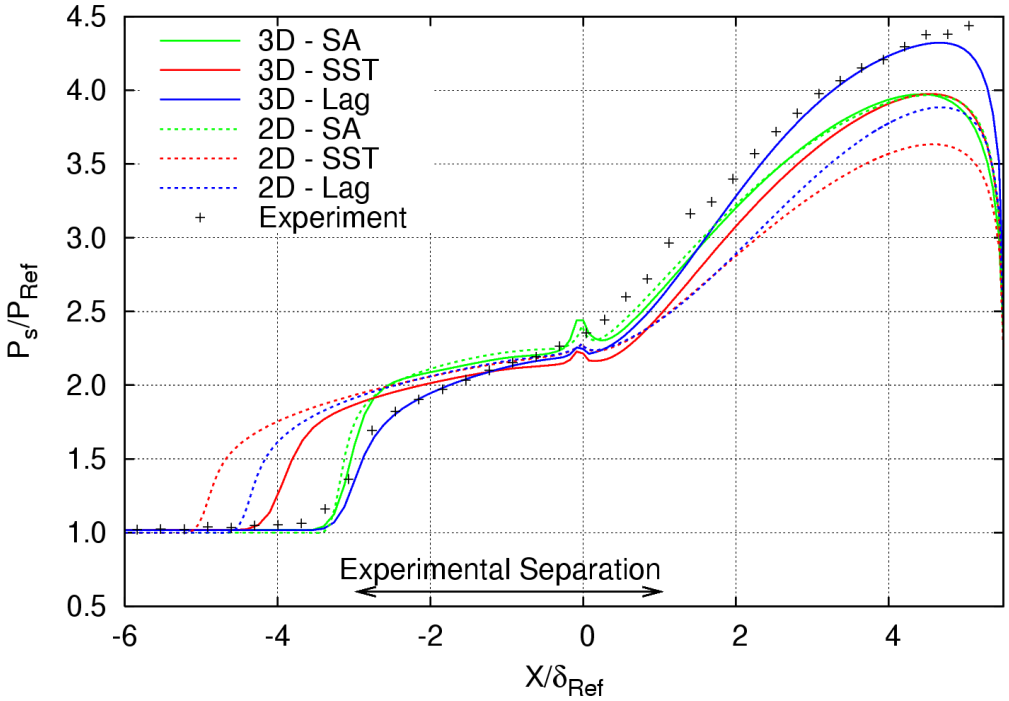

Figure 14. Surface pressure distribution along centerline of Kuntz 24° ramp.